Quantitative 3D analysis of tissue damage in a rat model of microembolization

Georgakopoulou, T.; van der Wijk, A.-E.; Bakker, E.N.T.P.; vanBavel, E.; INSIST investigators

DOI
10.1016/j.jbiomech.2021.110723

Publication date
2021

Document Version
Final published version

Published in
Journal of Biomechanics

License
CC BY

Journal of Biomechanics 128 (2021) 110723

Contents lists available at ScienceDirect

Journal of Biomechanics

journal homepage: www.elsevier.com/locate/jbiomech

Quantitative 3D analysis of tissue damage in a rat model of microembolization

Theodosia Georgakopoulou [a], Anne-Eva van der Wijk [a], Erik N.T.P. Bakker [a], Ed vanBavel [a,*], on behalf of the INSIST investigators

[a] Amsterdam University Medical Centers, University of Amsterdam, Biomedical Engineering and Physics, Amsterdam Cardiovascular Sciences, Meibergdreef 9, Amsterdam, The Netherlands

ARTICLE INFO

Keywords:
Stroke
Endovascular therapy
Incomplete microvascular reperfusion
Microembolization
Hypoxia
Spatial analysis

ABSTRACT

There is a discrepancy between successful recanalization and good clinical outcome after endovascular treatment (EVT) in acute ischemic stroke patients. During removal of a thrombus, a shower of microemboli may release and lodge to the distal circulation. The objective of this study was to determine the extent of damage on brain tissue caused by microemboli. In a rat model of microembolization, a mixture of microsphere (MS) sizes (15, 25 and 50 μm diameter) was injected via the left internal carotid artery. A 3D image of the left hemisphere was reconstructed and a point-pattern spatial analysis was applied based on G- and K-functions to unravel the spatial correlation between MS and the induced hypoxia or infarction. We show a spatial correlation between MS and hypoxia or infarction spreading up to a distance of 1000–1500 μm. These results imply that microemboli, which individually may not always be harmful, can interact and result in local areas of hypoxia or even infarction when lodged in large numbers.

1. Introduction

Among cardiovascular diseases, stroke is the second leading cause of death and the third leading cause of disability worldwide. Acute ischemic stroke (AIS; i.e. thrombotic or embolic occlusion of a cerebral artery) accounts for about 80% of stroke cases (Bamford et al., 1991). In the past years, next to thrombolysis, endovascular treatment (EVT) has been included in the standard treatment of AIS. During EVT, the thrombus is removed by aspiration catheters or stent retrievers, more recently extended with proximal flow arrest and aspiration (Munich et al., 2019). EVT results in the majority of cases (up to 95%) in successful recanalization of the occluded vessel (Bhaskar et al., 2018). However, a large proportion of the patients (63%) has poor functional outcome (Wollenweber et al., 2019), which may be caused by suboptimal local perfusion of the brain tissue (Dankbaar et al., 2017).

Despite the improvement of EVT devices, embolization of the distal arterial bed by fragments of the initial thrombus might occur (Farina et al., 2018; Sheriff et al., 2020). This hypothesis is supported by in vitro models of EVT where during removal of a thrombus thousands of microemboli (<50 μm) release (Arslanian et al., 2019). While thrombolysis is performed prior to EVT in eligible patients (i.e. within 4.5 h after symptom onset (Wardlaw et al., 2012)), it is unclear whether all microemboli resulting from EVT are lysed (Broocks et al., 2021).

While occlusions caused by mm-size emboli will clearly contribute to poor reflow in the tissue downstream territory, it is much less clear what the effect is of the numerous small fragments. Given the syncytial nature of the capillary bed and the possibility for oxygen transfer by diffusion, the smallest fragments may be less harmful. Optimal design of clot retriever device therefore requires information on the effects of these smaller fragments. In particular, there is much attention for the development of in silico clinical trials on new intervention strategies in ischemic stroke (Konduri et al. (2020)). Such trials require a detailed and quantitative understanding of local tissue damage by microocclusions in order to contribute to the improvement of device design.

In a previous study, we found that polystyrene microspheres (MS) occlude arteriole-sized vessels in the brain, leading to tissue hypoxia and infarction after 24 h (Georgakopoulou et al., 2021). In the present study, we used this rat model of impermeable thrombi to quantify spatial characteristics of tissue damage following microembolization of the brain. We reconstructed a brain volume of the intervention hemisphere and segmented and quantified the brain damage. Subsequently, we studied the spatial distribution of microemboli and hypoxic or infarcted

* Corresponding author.
E-mail address: e.vanbavel@amsterdamumc.nl (E. vanBavel).

https://doi.org/10.1016/j.jbiomech.2021.110723
Accepted 25 August 2021
Available online 2 September 2021

regions and explored their spatial relationships in the brain.

2. Materials and methods

Detailed Methods, including all experimental procedures and the spatial analysis of MS and brain damage can be found in the Supplementary material.

In short, we injected MS in the brain of six rats (3 male, 3 female). Buprenorphine (Temgesic™, 0.05 mg/kg, Schering-Plough, Welwyn Garden City, Hertfordshire, UK) was used as analgesic and the animals

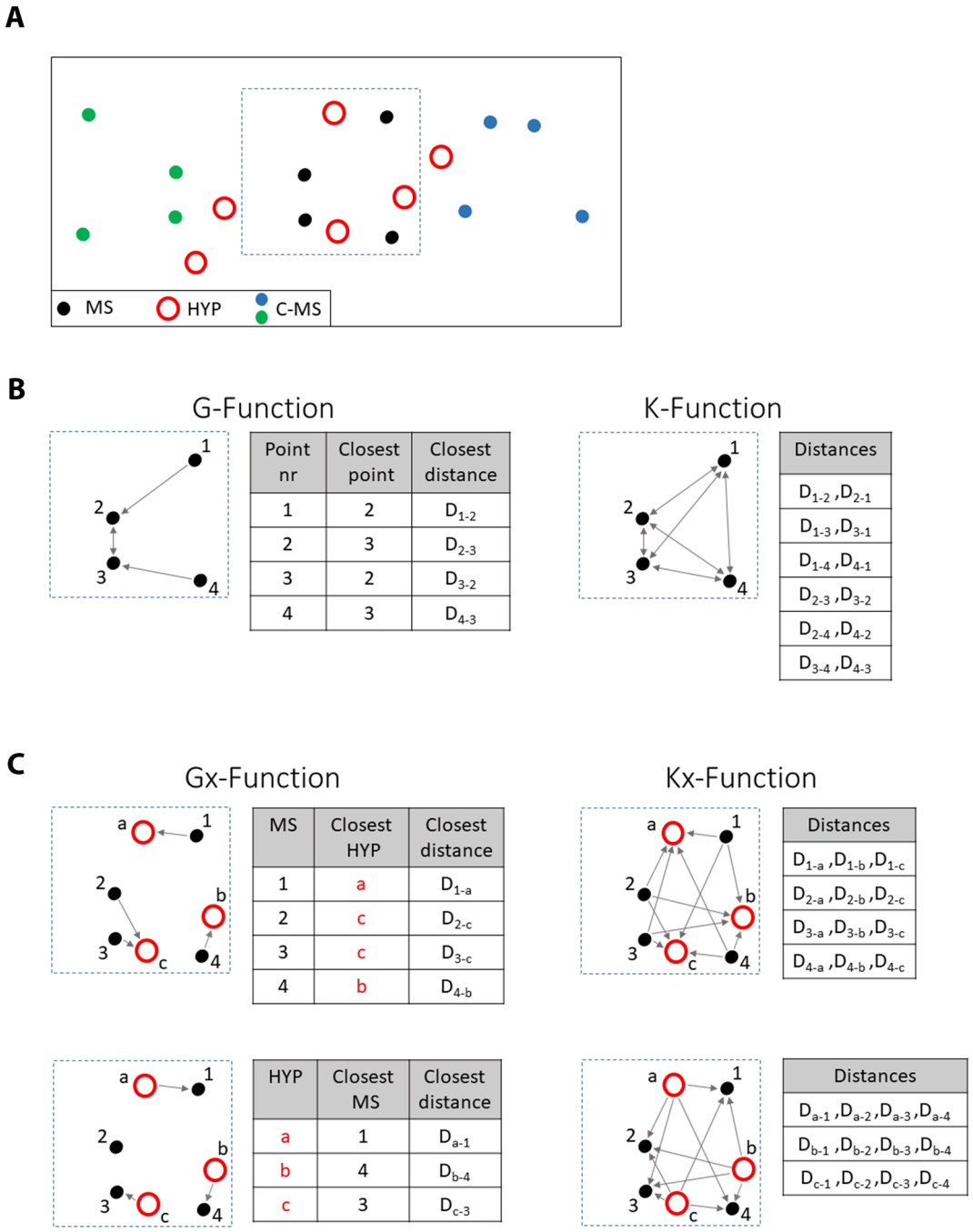

Fig. 1. Schematic explanation of spatial analysis. **(A)** The experimental data depicted as black filled circles (MS), and red open circles (HYP) and two scenarios of the generated data depicted as blue or green filled circles (C-MS). For the Monte-Carlo simulations, the generation of C-MS was repeated 250 times. Note that the generated C-MS have similar distribution of interparticle distances as the experimental MS data. G- and K-functions were used to describe the spatial relations within and between experimental and generated data. The experimental points within the dotted area are used to explain these functions in the following panels. **(B)** G-function: Per MS, the closest neighbor was detected and the distance (grey arrows) was determined as shown in the table. The G-function is the cumulative density function of these nearest neighbor distances. K-function: Grey arrows indicate the distances from all MS to all other MS (see table). The K-function is the cumulative density function of all these distances. **(C)** Gx-function: Grey arrows indicate distances from MS to their nearest HYP (upper panel) and vice versa (lower panel). Per MS or HYP, the closest neighbor is detected and the distance is determined as shown in the tables. The Gx-function is the cumulative density function of the nearest neighbor distances. Kx-function: arrows indicate distances from MS to all HYP (upper panel) and from HYP to all MS (lower panel). Note that for Kx but not Gx, the distances are the same whether measured from MS or HYP (see tables). The cumulative densities of all the distances are the Kx-function. MS: Microspheres,HYP: Hypoxic centroids, C-MS: Generated control points for MS.

were anesthetized with 2–2.5% isoflurane in 1 L/min O_2. The 3D spatial distribution of MS and centroids of hypoxic (HYP) and infarcted (INF) regions was tested using a point-pattern analysis based on the G- and K-functions (Fig. 1). These are cumulative density functions of respectively the nearest neighbor distances (NND) and all distances between point events. The point events could be homogeneous (e.g. only MS) or heterogeneous (e.g. MS and HYP). The latter are denoted as cross-G (Gx) and cross-K (Kx) functions. The experimental distributions were tested against Monte-Carlo simulations of control locations for MS or HYP based on null hypotheses (H_0).

Prior to the calculation of Gx- and Kx-functions, the spatial distribution of MS in the brain was tested. Thereto, MS distributions were compared to the H_0 of purely randomly dispersed points, generated with Monte-Carlo simulations. As this analysis showed significant clustering of MS in the brain tissue, we generated control locations (C-MS) with similar G- and K-functions as the MS. The same procedure was repeated for the generation of control points representing HYP (C-HYP). These generated clustered control points were then used to evaluate the spatial relation between MS and HYP based on the Gx- and Kx-functions. For the spatial relation between MS and INF, the analysis was limited to the calculation of Gx- and Kx-functions for distances from INF to either MS or C-MS, due to the low INF numbers.

3. Results

3.1. Stochastic nature of MS-induced hypoxic regions distribution

Fig. 2 provides an example of the distribution of MS and their effect on local hypoxia. Fig. 2C demonstrates a 50-μm thick section, with clearly discernible MS and demarcated zones of hypoxia. Fig. 2D shows x and y coordinates of MS and HYP, based on the full stacked image of 10 consecutive histological sections, totaling 500 μm. As can be seen, the spatial relationship between MS and the consequent hypoxia appeared to be quite diffuse, rather than a one-on-one relationship between MS and hypoxic regions in the near vicinity. In addition, MS appeared to be clustered.

3.2. Size distribution of hypoxic and infarcted regions

The number of MS that reached the brain varied between animals, ranging from 43 to 190 per reconstructed brain volume (Table 1 and Supplementary table 1). All animals had signs of hypoxia and infarction (Table 1 and Supplementary Fig. 1). On average, 82 ± 41 hypoxic regions and 4 ± 2 infarctions were detected in the reconstructed hemispheres. Only 10% of the hypoxic regions was ≥ 0.01 mm^3, whereas the majority of infarcted regions was ≥ 0.01 mm^3 (Fig. 3A) and infarctions

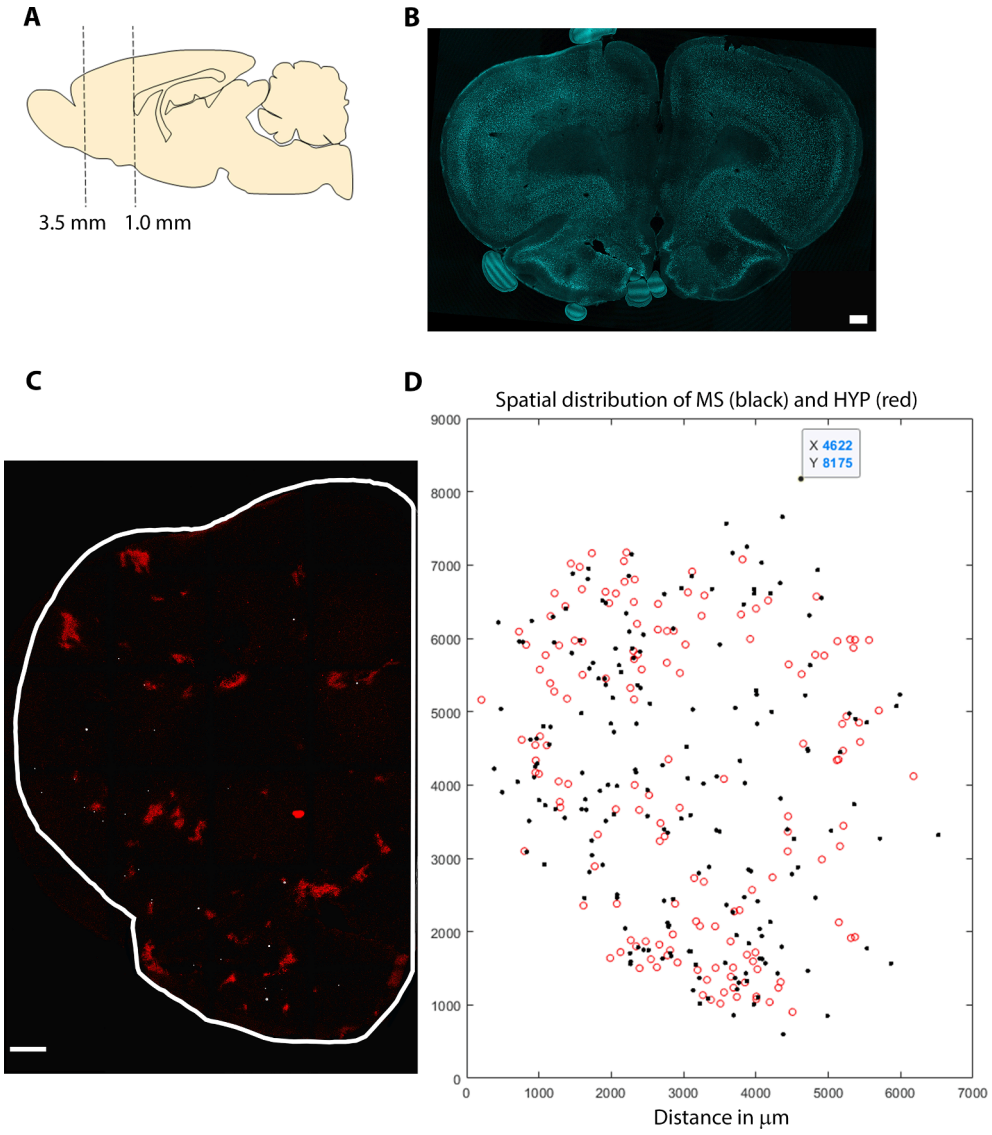

Fig. 2. **(A)** Schematic drawing of a rat brain. Dashed lines indicate the bregma coordinates where the brain sections were made. Only ten consecutive sections were selected for the reconstruction of the brain volume. **(B)** A representative 50-μm thick coronal section stained with NeuN antibody indicating the anatomy of the brain structures. Scale bar 500 μm. **(C)** A maximum intensity projection of the same 50-μm thick coronal section as in (B) of only the intervention hemisphere. Distribution of MS (white dots) of different sizes and hypoxic regions (red). Scale bar 500 μm. **(D)** Spatial 2D distribution of MS (black points) and HYP (red circles) of a reconstructed brain hemisphere (500 μm thick). MS: Microspheres, HYP: Hypoxic centroids.

Table 1
Number and density of MS lodged in 500 μm-thick reconstructed brain volumes and the numbers of the hypoxic and infarcted regions per animal (N = 6 animals). MS: Microspheres.

Animal #	Number of lodgded MS/ (MS density (MS/mm^3))	Number of hypoxic regions	Number of infarcted regions
1	190/(10.6)	152	5
2	81/(4.9)	83	2
3	43/(2.3)	27	6
4	79/(4.3)	70	1
5	115/(5.9)	67	4
6	105/(3.9)	94	4

were ~ 30 times larger in size (Fig. 3B).

3.3. Correlation between MS density and brain damage

Considering the variable number of MS detected in the brain between animals, we assessed whether there is a correlation between MS density and 1) the total volume and 2) the number of hypoxic and infarcted regions. Fig. 4A shows a positive correlation between MS density and hypoxia, both in terms of number of hypoxic regions and hypoxic volume (Fig. 4A; left graph: Pearson $R^2 = 0.87$, $P = 0.024$ and right graph: Pearson $R^2 = 0.91$, $P = 0.003$). In contrast, MS density was not correlated with the number of infarcted regions (Fig. 4B; left graph: Pearson $R^2 = 0.02$, $P = 0.809$), nor with the total infarcted volume (Fig. 4B; right graph: Pearson $R^2 = 0.51$, $P = 0.111$).

Notably, the total infarcted volume correlated with the total hypoxic volume (Fig. 4C Pearson $R^2 = 0.51$, $P = 0.042$).

3.4. Point-pattern spatial analysis of MS and tissue hypoxia or infarction

Based on the above observations, we conducted a point-pattern spatial statistical analysis of our data. First, we tested whether MS or HYP were clustered. Fig. 5A-B shows representative G- and K-functions (black) of the experimental spatial distributions of MS. Also shown are the G- and K-functions of fully randomly distributed control points (blue), generated by Monte-Carlo simulations (250 repeats). All functions were left-shifted as compared to the random controls, indicating that MS locations were clustered in this example. The curves were significantly different over a large distance range (Fischer's method, n = 6 animals, data not shown). The same analysis was done for HYP, with similar results (Fig. 5C-D; black and blue).

In order to analyze the spatial correlations between MS and HYP, we therefore attempted to generate clustered control points with equal G- and K-functions. As indicated by the mean and confidence interval of these generated clustered control points (Fig. 5A-D, magenta), tight matches of the G- and K-functions to the experimental data were obtained. Fig. 5E-F shows the mean NND of experimental data versus the clustered control points for the six animals. These distances were different between animals, related to the total number of MS and HYP. For five out of six experiments, the NND of the generated points tightly matched that of the data, with somewhat less matching in the sixth case.

Next, we set out to study the spatial relationship between MS and HYP, first by analyzing the distances from MS to HYP (Fig. 6A-B) and then from HYP to MS (Fig. 6C-D). Representative Gx- and Kx-functions of the experimental spatial distributions (black) between MS and HYP, versus the simulated spatial distributions (magenta) between C-MS and HYP are shown in Fig. 6A-B. Fig. 6A demonstrates substantial variation in experimental NND (black), with 50% of the closest HYP being further away than 200 μm from MS. Still, comparison to the Monte-Carlo simulations (magenta) that were based on absence of spatial correlation, revealed that HYP are closer to MS than to C-MS. This indicates a spatial correlation between MS and their closest HYP for this example. Spatial correlation was also confirmed in the Kx-function between MS and all HYP, as shown in Fig. 6B. There, the experimental spatial distribution of

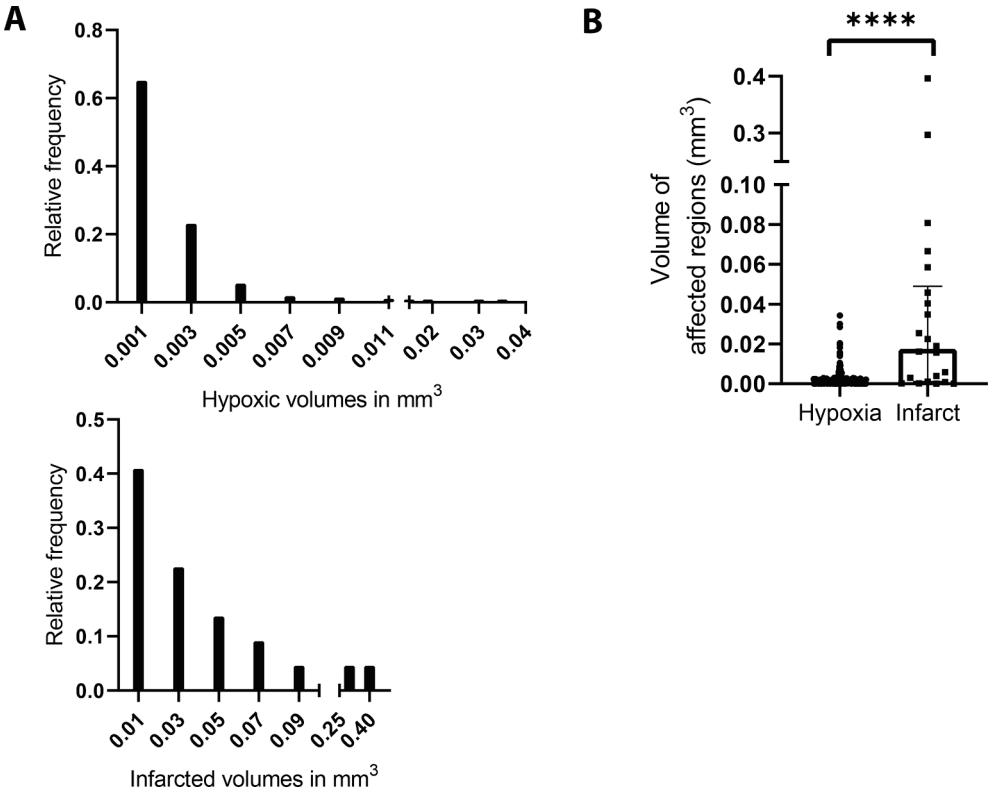

Fig. 3. Comparison between hypoxic and infarcted regions. **(A)** Size distribution of hypoxic (upper graph) and infarcted (lower graph) regions, as measured in a 500-μm reconstructed volume of the intervention hemisphere. **(B)** Hypoxic regions caused by microembolization are significantly smaller than the infarcted regions. Data are depicted as median with interquartile range. ****$P < 0.0001$, Mann-Whitney. Pooled data from six animals (N = 6).

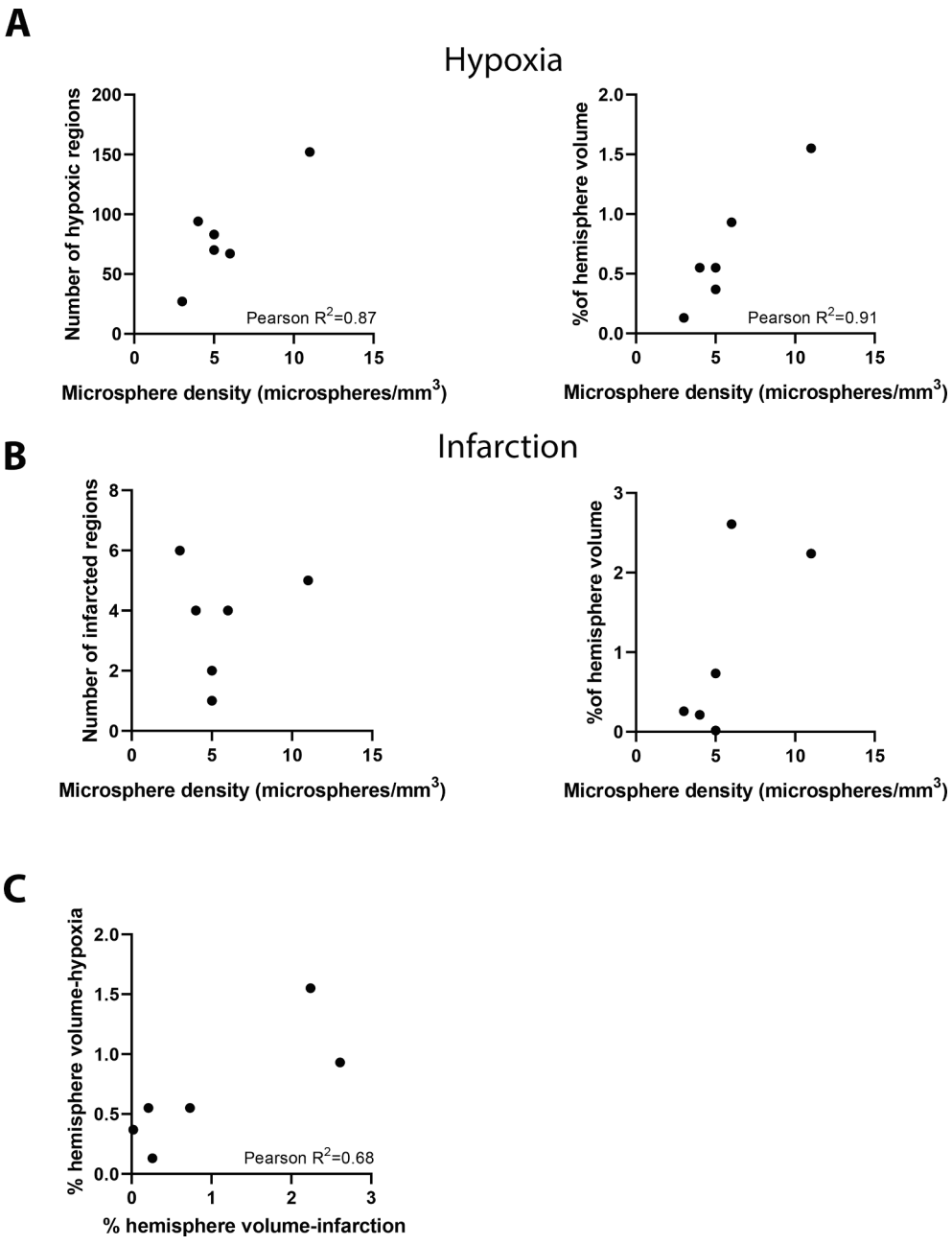

Fig. 4. Correlation between MS density and number or total volume of hypoxic or infarcted regions in a 500-μm reconstructed volume of the intervention hemisphere. **(A)** Significant positive correlation between MS density and number (left graph; Pearson's correlation coefficient, $R^2 = 0.87$, *P = 0.024) or total volume of hypoxic regions (right graph; Pearson's correlation coefficient, $R^2 = 0.91$, **P < 0.001). **(B)** No significant correlation between MS density and the number (left graph) or total volume (right graph) of infarcted regions. **(C)** Significant positive correlation between total hypoxic volume and total infarcted volume (Pearson's correlation coefficient, $R^2 = 0.68$, *P = 0.042). N = 6 animals. MS: Microspheres.

distances between MS and HYP (black), was left-shifted compared to the simulated data (magenta) up to tested distances of 2000 μm. Similar results were found in the reverse distance analysis, from HYP to either their closest MS (Fig. 6C), or all MS (Fig. 6D) for this particular example. Fig. 6E-F shows the mean NND of experimental data versus the Monte-Carlo simulated data for the six animals. Pairwise comparison of mean NND of MS or C-MS to HYP indicates that the closest HYP were on average 388.7 ± 107.2 μm closer to MS than control points (Fig. 6E; P = 0.0003, paired *t*-test). MS were found to be on average 332.2 ± 86.7 μm closer to HYP than control points (Fig. 6F; P = 0.0002, paired *t*-test).

Fig. 7 shows the difference between experimental Gx- and Kx-functions and their Monte-Carlo simulations for the six animals (ΔGx and ΔKx respectively). ΔGx was significantly positive up to the tested distance of 800 μm (Fig. 7A). Note that the majority of MS and HYP clustering took place within the first 200 μm. ΔKx was significantly positive up to the tested distance of 2000 μm, with the plateau around 1500 μm (Fig. 7B). Similar spatial correlations were found for the reverse analysis of MS to their closest HYP (Fig. 7C) or all HYP (Fig. 7D). Taken together, the above data demonstrate a spatial correlation over hundreds of micrometers between MS and HYP.

Lastly, we tested the spatial relation between MS and INF. Fig. 8 shows the ΔGx and ΔKx curves for the six animals, between experimental data and their Monte-Carlo simulations. Fig. 8A shows that clustering of INF and their closest MS, is maximal at a distance of 200 μm. Fig. 8B shows a correlation between MS and INF up to a distance of 2000 μm with a maximum at 1000 μm.

4. Discussion

Our study addressed effects of microvascular occlusions as could occur after EVT, and provides quantitative spatial data on tissue hypoxia and infarction. In particular, we found that microembolization caused numerous hypoxic and a few infarcted regions, in the wide vicinity around lodged MS. The effects of MS were highly stochastic in nature,

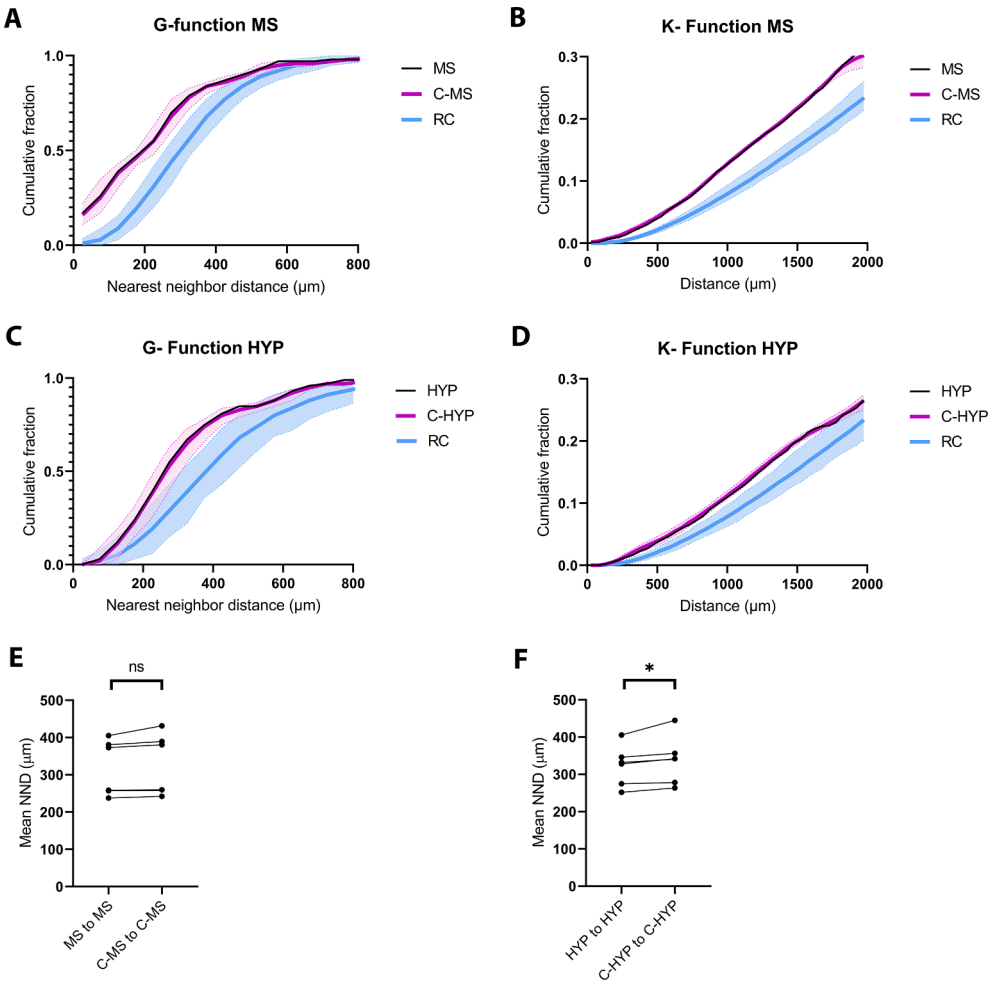

Fig. 5. Representative example of MS or HYP clustering and generation of 'clustered' control points for MS and HYP. **(A)** G-Function: Cumulative densities of NND between MS (black curve; experimental data) versus RC (blue curve, simulated data) and C-MS (magenta curve; simulated data). **(B)** K-Function: Cumulative densities of distances between all MS versus RC and C-MS. **(C)** G-Function: Cumulative densities of NND between HYP versus RC and C-HYP. **(D)** K-Function: Cumulative densities of distances between all HYP versus RC or C-HYP. **(E,F)** Pairwise comparisons of mean NND between experimental data and C-MS or C-HYP. Lines connect dots corresponding to mean NND measured in the intervention hemisphere of the same individual rats. ns = not significant, *P < 0.05 paired *t*-test, N = 6 animals. The filled area indicates confidence intervals. RC: Randomly generated (i.e. with homogeneous probability over the tissue and independently from each other) control points, MS: Microspheres, C-MS: Control points for MS, HYP: Hypoxic centroids, C-HYP: Control points for HYP, NND: Nearest neighbor distances.

with respect to both volume of affected tissue and distance from MS. A point-pattern analysis between MS and HYP or INF revealed a spatial correlation over hundreds of micrometers. To our knowledge, these data are unique and map the complex interactions of multiple arterial occlusions due to lodged MS.

4.1. Justification of spatial analysis and interpretation of spatial correlations

The relationship between occlusion and brain damage is complex and depends on the geometry of the vascular bed. A shower of microemboli sized between 15 μm and 50 μm targets the vascular bed at the level of penetrating arteries, arterioles and capillaries. Penetrating arteries (20–90 μm diameter) bridge the pial vascular network of the brain surface with the intracortical microvascular network (7–20 μm diameter) (Ngai and Winn, 1995). In contrast to the highly anastomosing architecture of both the pial and intracortical vascular networks, the penetrating arteries are mostly lacking anastomoses (Nishimura et al., 2007). Thus, occlusions in the network at particularly this level, because of a microembolic shower, could lead to blood flow reduction and microinfarcts.

In order to determine the spatial relationship of MS with damage resulting from obstruction of the microvasculature, we applied a point-pattern spatial analysis. The difference of the Gx-functions from their Monte-Carlo simulations, which assumed no relation between MS and hypoxic regions, was maximal for NND of ~ 200 μm (Fig. 7A,C). This indicates that a single MS induces a risk for hypoxia in a surrounding tissue sphere that extents up to this distance. For the Kx-function, the difference with the control (Fig. 7B,D) continued to increase up to the largest analyzed distance of 2000 μm, with most of the effect up to ~ 1500 μm. This shows that up to this distance the number of MS surrounding hypoxic areas was larger than expected based on uncorrelated distributions of spheres and hypoxic areas and that even distant MS still may cause tissue hypoxia. In an attempt to explain these results, we propose that risk zones of two or more MS extend towards each other. Fig. 9 provides a schematic representation of this effect. Such a cooperative effect of multiple MS could relate to the blocking of the vascular bed at multiple entrance vessels to a tissue area that then becomes hypoxic. These entrance vessels could be arterioles, small local collaterals or part of the continuous capillary bed. However, a more careful interpretation of the current data requires simulation of these processes, based on vascular topology data.

We included in our analysis three MS sizes, which in turn block the vessels at different levels and thus most likely exert their effects to different distances relative to the site of occlusion (Hamilton et al., 2010). Tissue damage resulting from microvascular occlusions depends on the clot location. Thus, it has been shown that occlusion of a single pial vessel or a single capillary results in focal ischemia and is rather harmless (Schaffer et al., 2006; Shih et al., 2013). In contrast, penetrating vessels are a critical bottleneck in cortical blood flow, affecting blood flow in a large region downstream of an occlusion (Nishimura et al., 2007) and leading to microinfarcts (Shih et al., 2013). Data coming from single penetrating artery occlusions show that brain damage spans up to a radius of ~ 230 μm and a depth of ~ 1200 μm relative to the pial surface (cortical columns) (Shih et al., 2013). The radii of influence found in the current study are of the same order. One

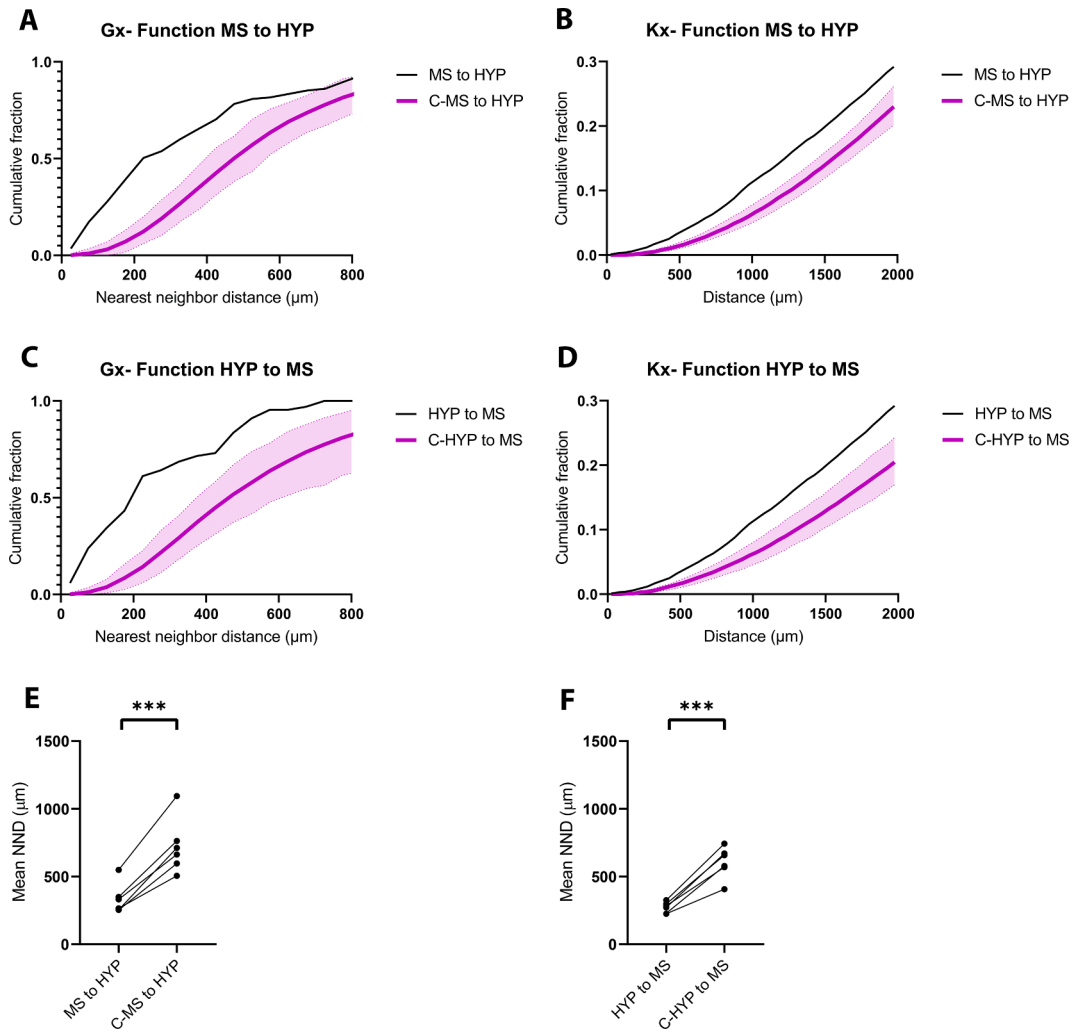

Fig. 6. Representative examples of clustering between MS and HYP and pairwise comparisons of mean NND. **(A)** Gx-Function: Cumulative densities of NND between MS and HYP (black curve; experimental data) and between C-MS and HYP (magenta curve; simulated data). **(B)** Kx-Function: Cumulative densities of distances between all MS and HYP and between all C-MS and HYP. Note, Kx-Function for distances between all MS and HYP is the same as HYP and MS. **(C)** Gx-Function: Cumulative densities of NND between HYP and MS and between C-HYP and MS. **(D)** Kx-Function: Cumulative densities of distances between all HYP and MS and between all C- HYP and MS. **(E, F)** Pairwise comparisons between mean NND from MS or C-MS to HYP and between mean NND from HYP or C-HYP to MS. Lines connect dots corresponding to NND measured in the intervention hemisphere of the same individual rats. ***P < 0.001 paired *t*-test, N $= 6$ animals. The filled area indicates confidence intervals. MS: Microspheres, C-MS: Control points for MS, HYP: Hypoxic centroids, C-HYP: Control points for HYP, NND: Nearest neighbor distances.

might suspect that the extent of the brain damage caused by the largest MS could partly explain the large radii found here, in the sense that the damage caused by the larger may overshadow the effect of the smaller ones. However, we believe that this is highly unlikely, firstly because the majority of MS in our model is of 15 μm and secondly due to the shape and distribution of hypoxic regions in the intervention hemisphere, where they do not necessarily originate from the brain surface as cortical column-shaped regions. Consequently, we believe that there is a cooperative effect between the smaller MS, which spreads in the brain tissue. In a future study, we aim to isolate the effect of different MS sizes on brain tissue damage by injecting each MS size separately per group.

In addition to the high number of hypoxic regions, we observed a few much larger infarcted regions. MS were clustered around infarcts, with Gx- and Kx-functions (Fig. 8) that resemble those of the hypoxic areas (Fig. 7), and we suggest that also the infarct zones were caused by the interactive effects of multiple MS in the wide surrounding. The large size and small number suggest that the infarcted regions develop from merging hypoxic zones. Yet, it is not obvious from the data if and how the local and more remote MS affect this process.

4.2. Limitations of the study

We investigated hypoxia and infarction only at 24 h after micro-embolization. Other timepoints could provide insight into the progression of hypoxia towards infarction or recovery. Of interest, in a previous study, total hypoxic volume became less after 7 days, without a growth in infarct volume in this micro-embolization model, pointing at recovery (Georgakopoulou et al., 2021). For the full analysis and understanding of such events several factors should be taken into account, in addition to the size and number of MS (Tsai et al., 2011). These include the arterial topology and notably the percentage of anastomosing arteries per arterial level (Ngai and Winn, 1995). Although the segmentation of the numerous arterioles and capillaries and the generation of reliable connectivity between these segments are major technical obstacles, microvascular network data could help building more detailed mechanistic models. Moreover, further experimental work is needed. We are currently developing techniques for clearing of brain tissue and 3D imaging of much larger volumes by light sheet microscopy (Lugo-Hernandez et al., 2017; Zhang et al., 2018). Another aspect not addressed in the current study is the differential vulnerability of brain regions to an

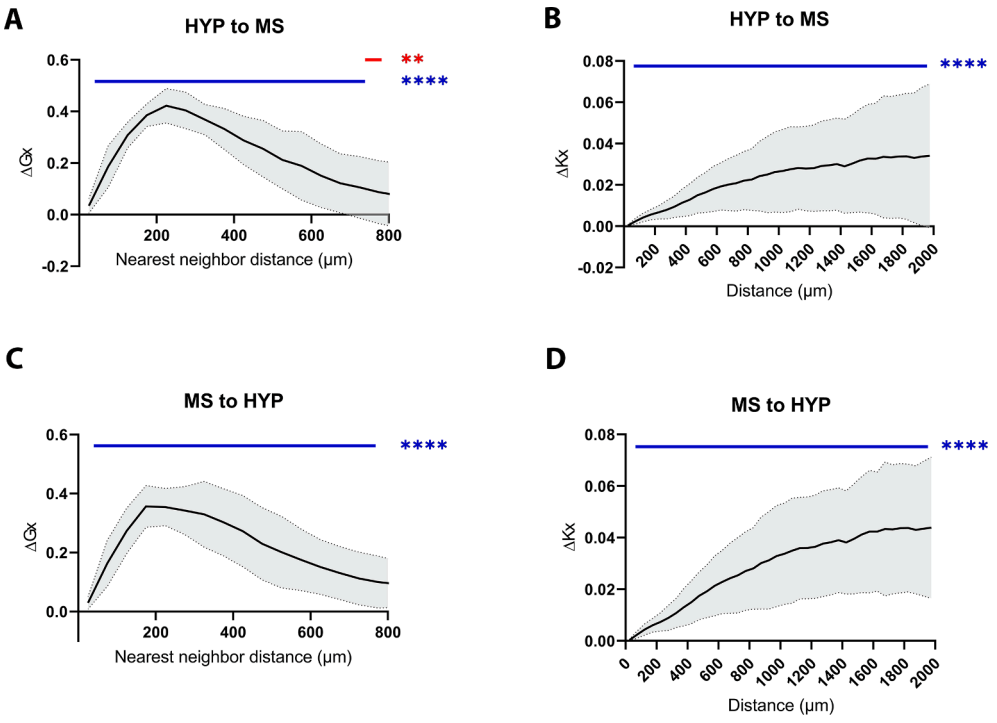

Fig. 7. Experimental data minus average of Monte-Carlo simulations. **(A)** ΔGx-Function: Cumulative densities of NND between HYP and MS (experimental data) minus mean cumulative densities of NND between C-HYP and MS (simulated data, assuming no relation between MS and HYP). **(B)** ΔKx-Function: Cumulative densities of distances between all HYP and MS (experimental data) minus mean cumulative densities of distances between all C-HYP and MS (simulated data). **(C)** ΔGx-Function: Cumulative densities of NND between MS and HYP (experimental data) minus mean cumulative densities of NND between C-MS and HYP (simulated data). **(D)** ΔKx-Function: Cumulative densities of distances between all MS and HYP (experimental data) minus mean cumulative densities of distances between all C-MS and HYP (simulated data). The filled area indicates standard deviation for the ΔGx- or ΔKx-functions over the six animals. The data in B and D are equal by definition, but the Monte-Carlo simulations are not. MS: Microspheres, C-MS: Generated control for MS, HYP: Hypoxic centroids, C-HYP: Generated control for HYP, NND: Nearest neighbor distances. **P < 0.01(red parallel lines above the curve indicate to which distance interval the significance of the data is **P < 0.01), ****P < 0.0001(blue parallel lines above the curve indicate to which distance interval the significance of the data is ****P < 0.0001) Fischer's method p-value, N = 6 animals.

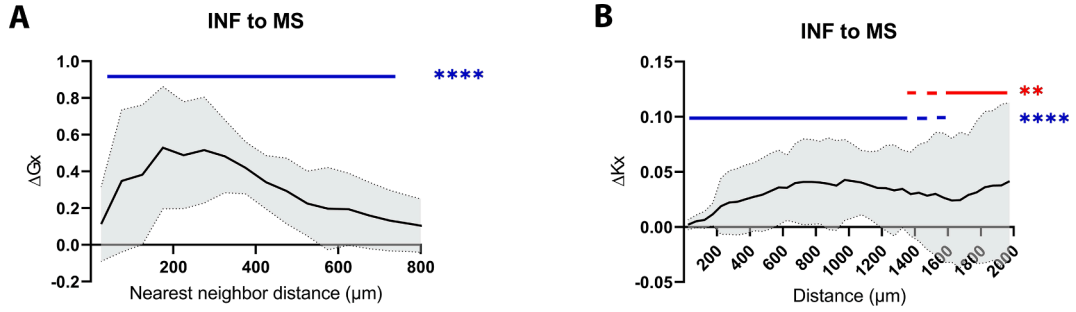

Fig. 8. Experimental data minus average of Monte-Carlo simulations. **(A)** ΔGx-Function: Cumulative densities of NND between INF and MS (experimental data) minus mean cumulative densities of NND between INF and C-MS (simulated data). **(B)** ΔKx-Function: Cumulative densities of distances between all INF and MS (experimental data) minus mean cumulative densities of distances between all INF and C-MS (simulated data). The filled area indicates standard deviation for the ΔGx- or ΔKx-functions over the six animals. MS: Microspheres, INF: Infarcted centroids, C-MS: Generated control points for MS, NND: Nearest neighbor distances. **P < 0.01(red lines above the curve indicate to which distance interval the significance of the data is **P < 0.01), ****P < 0.0001(blue lines above the curve indicate to which distance interval the significance of the data is ****P < 0.0001) Fischer's method p-value, N = 6 animals.

ischemic environment (Pulsinelli et al., 1982; Xu et al., 2001), notably the difference between gray and white matter.

When we designed these experiments, we expected to find a much more localized spatial relation between lodged MS and the induced hypoxic and infarcted areas. We do not believe that the wide dispersion results from experimental noise. Thus, as shown in Fig. 2 the hypoxia staining is characterized by clearly discernable zones. While the estimated number and volumes of these hypoxic regions depend on segmentation choices, the stochastic nature of the spatial correlations is expected to be rather insensitive to the segmentation procedure. Indeed, in an alternative approach (not shown) we determined mean hypoxia fluorescence as a function of distance from the MS on a pixel basis, avoiding the need for segmentation. This resulted in a profile that is consistent with the Kx-function. It remains to be tested whether the stochastic effects of lodged MS are homogeneous over the tissue and equal in all directions

Since we used tissue volumes of 500-μm in thickness, we expect that MS outside this volume have influenced the hypoxia and infarct patterns. The contribution of these MS is hard to establish, but is expected to add noise to spatial relationships when considering larger distances. Some care should therefore be taken in interpretation of the distribution functions at large distances. At small distances, where these boundary effects are less relevant, we found clear differences in the Gx- and Kx-functions compared to those of the control points. We therefore suggest that the stochastic spatial relation between lodged MS and hypoxia is a direct consequence of the effects of the MS on perfusion, with resulting hypoxia depending on the balance of oxygen delivery (by remaining perfusion or diffusion) and oxygen consumption (Leithner

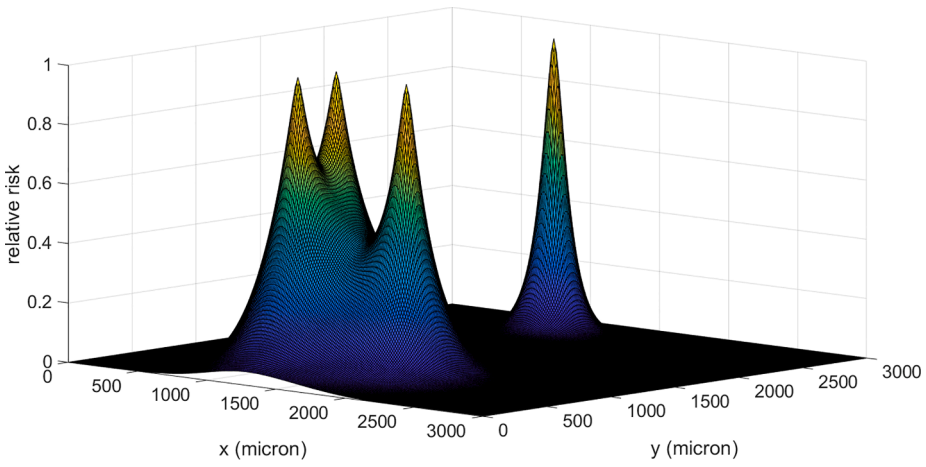

Fig. 9. Illustration of the spatial analysis interpretation. Indicated is the combined effect of four MS on the risk of developing hypoxia in the surrounding tissue. Each MS induces a risk that becomes smaller with increasing distance. An isolated MS at the right causes a risk for hypoxia that extends to around 200 μm, explaining the ΔGx-function. Three relatively close MS on the left generate a much broader risk profile, reflecting a collaborative effect and explaining the shallow and extended ΔKx-function.

and Royl, 2014).

The spatial distribution analysis between homogeneous point events showed clustering of MS. This complicated the statistical analysis but we believe that by including clustering in the Monte-Carlo simulations we adequately accounted for this. Numerous studies in the past applied MS infusion in order to determine the flow distribution in the brain and other organs (Prinzen and Bassingthwaighte, 2000) and showed regional cerebral blood flow variations (Horton et al., 1980). The fact that MS are distributed according to the flow, together with the heterogeneity in vascular density between gray and white matter (Cavaglia et al., 2001), could partly explain why MS were clustered. Since we compensate for clustering among MS in our analysis, possible fluctuations of the cerebral blood flow due to isoflurane-induced vasodilation (during MS injection), are not very likely to affect the spatial relation between MS and induced brain damage.

The number of MS found in the brain varied between the animals. We believe that this may be caused by the temporal ligation of external carotid artery and lifting of the common carotid artery (with a suture placed under it) during the surgery. Even though it is hard to trace back all injected MS, we believe that this intervention may have temporarily led to blood flow redistribution between the brain regions, or partial reflux of MS after the injection.

The variation in the number of lodged MS between the animals had an effect on the extent of the brain damage. Therefore, we checked the correlation between MS density and resulting brain damage and found significant positive correlation for hypoxia, but not for infarction. Since the varying number of MS affects both the number and total volume of hypoxic regions, it seems that the numerous but smaller MS sizes also contribute to the generation of local hypoxia. The absence of correlation between MS density and the number of infarcted regions could be attributed to the low number of infarcted regions and the low number of experiments (N = 6). However, there is a trend to positive correlation between MS density and total infarcted volume, though not significant (Fig. 4B right graph) and a significant correlation between total infarcted and total hypoxic volume (Fig. 4C).

5. Conclusion

We applied a 'black box' analysis of MS effects on brain tissue. We found that these MS have very stochastic effects on brain tissue over a relatively large distance, with an amplified effect of multiple MS. This work provides quantitative data on MS-induced tissue hypoxia and infarction that could serve for building in silico models of stent retrievers and aspiration catheters, which can be used for platforms like IN Silico trials for treatment of acute Ischemic STroke (INSIST).

Declaration of Competing Interest

The authors declare that they have no known competing financial interests or personal relationships that could have appeared to influence the work reported in this paper.

Acknowledgements

Sources of funding.

This project was funded from the European Union's Horizon 2020 research and innovation program under grant agreement No 777072 (INSIST). AEvdW was funded by Neuroscience Amsterdam (project number NDIS-2019-03)

Author contributions.

Declaration of Competing Interest.

The authors declare that the research was conducted in the absence of any commercial or financial relationships that could be construed as a potential conflict of interest.

ENTPB, EvB, AEvdW and TG designed the experiments; TG and AEvdW performed the surgeries; TG and EvB analyzed the data and wrote the manuscript; AEvdW, ENTPB and EvB contributed to editing of the manuscript. All authors read and approved the final version of the manuscript.

Appendix A. Supplementary data

Supplementary data to this article can be found online at https://doi.org/10.1016/j.jbiomech.2021.110723.

References

Arslanian, R.A., Marosfoi, M., Caroff, J., King, R.M., Raskett, C., Puri, A.S., Gounis, M.J., Chueh, J.-Y., 2019. Complete clot ingestion with cyclical ADAPT increases first-pass recanalization and reduces distal embolization. Journal of neurointerventional surgery 11 (9), 931–936.

Bamford, J., Sandercock, P., Dennis, M., Warlow, C., Burn, J., 1991. Classification and natural history of clinically identifiable subtypes of cerebral infarction. Lancet (London, England) 337 (8756), 1521–1526.

Bhaskar, S., Stanwell, P., Cordato, D., Attia, J., Levi, C., 2018. Reperfusion therapy in acute ischemic stroke: dawn of a new era? BMC neurology 18, 8.

Broocks, G., Meyer, L., Kabiri, R., Kniep, H.C., McDonough, R., Bechstein, M., van Horn, N., Lindner, T., Sedlacik, J., Cheng, B., Thomalla, G., Schön, G., Fiehler, J., Hanning, U., Schönfeld, M.H., 2021. Impact of intravenous alteplase on subangiographic emboli in high-resolution diffusion-weighted imaging following successful thrombectomy. Eur Radiol.

Cavaglia, M., Dombrowski, S.M., Drazba, J., Vasanji, A., Bokesch, P.M., Janigro, D., 2001. Regional variation in brain capillary density and vascular response to ischemia. Brain Res. 910 (1-2), 81–93.

Dankbaar, J.W., Horsch, A.D., van den Hoven, A.F., Kappelle, L.J., van der Schaaf, I.C., van Seeters, T., Velthuis, B.K., 2017. Prediction of Clinical Outcome After Acute Ischemic Stroke: The Value of Repeated Noncontrast Computed Tomography,

Computed Tomographic Angiography, and Computed Tomographic Perfusion. Stroke 48 (9), 2593–2596.
Farina, F., Palmieri, A., Favaretto, S., Viaro, F., Cester, G., Causin, F., Baracchini, C., 2018. Prognostic Role of Microembolic Signals After Endovascular Treatment in Anterior Circulation Ischemic Stroke Patients. World Neurosurg 110, e882–e889.
Georgakopoulou, T., van der Wijk, A.-E., Bakker, E.N.T.P., vanBavel, E.d., 2021. Recovery of Hypoxic Regions in a Rat Model of Microembolism. J Stroke Cerebrovasc Dis 30 (6), 105739. https://doi.org/10.1016/j.jstrokecerebrovasdis.2021.105739.
Hamilton, N.B., Attwell, D., Hall, C.N., 2010. Pericyte-mediated regulation of capillary diameter: a component of neurovascular coupling in health and disease. Front Neuroenergetics 2.
Horton, R.W., Pedley, T.A., Meldrum, B.S., 1980. Regional cerebral blood flow in the rat as determined by particle distribution and by diffusible tracer. Stroke 11, 39-44.
Konduri, P.R., Marquering, H.A., van Bavel, E.E., Hoekstra, A., Majoie, C.B.L.M., , T.I.I., 2020. In-Silico Trials for Treatment of Acute Ischemic Stroke. Frontiers in neurology 11.
Leithner, C., Royl, G., 2014. The oxygen paradox of neurovascular coupling. Journal of cerebral blood flow and metabolism : official journal of the International Society of Cerebral Blood Flow and Metabolism 34 (1), 19–29.
Lugo-Hernandez, E., Squire, A., Hagemann, N., Brenzel, A., Sardari, M., Schlechter, J., Sanchez-Mendoza, E.H., Gunzer, M., Faissner, A., Hermann, D.M., 2017. 3D visualization and quantification of microvessels in the whole ischemic mouse brain using solvent-based clearing and light sheet microscopy. Journal of cerebral blood flow and metabolism : official journal of the International Society of Cerebral Blood Flow and Metabolism 37 (10), 3355–3367.
Munich, S.A., Vakharia, K., Levy, E.I., 2019. Overview of Mechanical Thrombectomy Techniques. Neurosurgery 85, S60-s67.
Ngai, A.C., Winn, H.R., 1995. Modulation of cerebral arteriolar diameter by intraluminal flow and pressure. Circ Res 77 (4), 832–840.
Nishimura, N., Schaffer, C.B., Friedman, B., Lyden, P.D., Kleinfeld, D., 2007. Penetrating arterioles are a bottleneck in the perfusion of neocortex. PNAS 104 (1), 365–370.
Prinzen, F.W., Bassingthwaighte, J.B., 2000. Blood flow distributions by microsphere deposition methods. Cardiovasc Res 45, 13–21.
Pulsinelli, W.A., Brierley, J.B., Plum, F., 1982. Temporal profile of neuronal damage in a model of transient forebrain ischemia. Ann. Neurol. 11 (5), 491–498.
Schaffer, C.B., Friedman, B., Nishimura, N., Schroeder, L.F., Tsai, P.S., Ebner, F.F., Lyden, P.D., Kleinfeld, D., Corbetta, M., 2006. Two-photon imaging of cortical surface microvessels reveals a robust redistribution in blood flow after vascular occlusion. PLoS Biol 4 (2), e22. https://doi.org/10.1371/journal.pbio.004002210.1371/journal.pbio.0040022.g00110.1371/journal.pbio.0040022.g00210.1371/journal.pbio.0040022.g00310.1371/journal.pbio.0040022.g00410.1371/journal.pbio.0040022.g00510.1371/journal.pbio.0040022.g00610.1371/journal.pbio.0040022.g00710.1371/journal.pbio.0040022.g00810.1371/journal.pbio.0040022.t00110.1371/journal.pbio.0040022.sg00110.1371/journal.pbio.0040022.sg00210.1371/journal.pbio.0040022.sg00310.1371/journal.pbio.0040022.sg00410.1371/journal.pbio.0040022.sg00510.1371/journal.pbio.0040022.sg00610.1371/journal.pbio.0040022.sg00710.1371/journal.pbio.0040022.sd00110.1371/journal.pbio.0040022.sv001.
Sheriff, F., Diz-Lopes, M., Khawaja, A., Sorond, F., Tan, C.O., Azevedo, E., Franceschini, M.A., Vaitkevicius, H., Li, K., Monk, A.D., Michaud, S.L., Feske, S.K., Castro, P., 2019. Microemboli After Successful Thrombectomy Do Not Affect Outcome but Predict New Embolic Events. Stroke, Strokeaha119025856.
Shih, A.Y., Blinder, P., Tsai, P.S., Friedman, B., Stanley, G., Lyden, P.D., Kleinfeld, D., 2013. The smallest stroke: occlusion of one penetrating vessel leads to infarction and a cognitive deficit. Nat. Neurosci. 16 (1), 55–63.
Tsai, M.-J., Tsai, Y.-H., Kuo, Y.-M., 2011. Characterization of the pattern of ischemic stroke induced by artificial particle embolization in the rat brain. Biomaterials 32 (27), 6381–6388.
Wardlaw, J.M., Murray, V., Berge, E., del Zoppo, G., Sandercock, P., Lindley, R.L., Cohen, G., 2012. Recombinant tissue plasminogen activator for acute ischaemic stroke: an updated systematic review and meta-analysis. Lancet (London, England) 379 (9834), 2364–2372.
Wollenweber, F.A., Tiedt, S., Alegiani, A., Alber, B., Bangard, C., Berrouschot, J., Bode, F. J., Boeckh-Behrens, T., Bohner, G., Bormann, A., Braun, M., Dorn, F., Eckert, B., Flottmann, F., Hamann, G.F., Henn, K.-H., Herzberg, M., Kastrup, A., Kellert, L., Kraemer, C., Krause, L., Lehm, M., Liman, J., Lowens, S., Mpotsaris, A., Papanagiotou, P., Petersen, M., Petzold, G.C., Pfeilschifter, W., Psychogios, M.-N., Reich, A., von Rennenberg, R., Röther, J., Schäfer, J.-H., Siebert, E., Siedow, A., Solymosi, L., Thonke, S., Wagner, M., Wunderlich, S., Zweynert, S., Nolte, C.H., Gerloff, C., Thomalla, G., Dichgans, M., Fiehler, J., 2019. Functional Outcome Following Stroke Thrombectomy in Clinical Practice. Stroke 50 (9), 2500–2506.
Xu, L., Sapolsky, R.M., Giffard, R.G., 2001. Differential sensitivity of murine astrocytes and neurons from different brain regions to injury. Exp. Neurol. 169 (2), 416–424.
Zhang, L.-Y., Lin, P., Pan, J., Ma, Y., Wei, Z., Jiang, L.u., Wang, L., Song, Y., Wang, Y., Zhang, Z., Jin, K., Wang, Q., Yang, G.-Y., 2018. CLARITY for High-resolution Imaging and Quantification of Vasculature in the Whole Mouse Brain. Aging Dis 9 (2), 262. https://doi.org/10.14336/AD.2017.0613.